Six-Plate Capacitive Coupler to Reduce Electric Field Emission in Large Air-Gap Capacitive Power Transfer

Hua Zhang, *Student Member, IEEE*, Fei Lu, *Student Member, IEEE*, Heath Hofmann, *Senior Member, IEEE*, Weiguo Liu, *Senior Member, IEEE*, and Chunting Chris Mi, *Fellow, IEEE*

***Abstract*—This paper proposes a six-plate capacitive coupler for large air-gap capacitive power transfer to reduce electric field emissions to the surrounding environment. Compared to the conventional four-plate horizontal structure, the six-plate coupler contains two additional plates above and below the inner four-plate coupler to provide a shielding effect. Since there is a capacitive coupling between every two plates, the six-plate coupler results in a circuit model consisting of 15 coupling capacitors. This complex model is first simplified to an equivalent three-port circuit model, and then to a two-port circuit model which is used in circuit analysis and parameter design. This six-plate coupler can eliminate the external parallel capacitor in the previous LCLC topology, which results in the LCL compensation and reduces the system cost. Due to the symmetry of the coupler structure, the voltage between shielding plates is limited, which reduces electric field emissions. Finite element analysis by Maxwell is used to simulate the coupling capacitors and electric field distribution. Compared to the four-plate horizontal and vertical structures, the six-plate coupler can significantly reduce electric field emissions and expand the safety area from 0.9 to 0.1 m away from the coupler in the well-aligned case. A 1.97 kW prototype is implemented to validate the six-plate coupler, which achieves a power density of 1.95 kW/m^2 and a dc–dc efficiency of 91.6% at an air-gap of 150 mm. Experiments also show that the output power maintains 65% of the well-aligned value at 300 mm *X* misalignment, and 49% at 300 mm *Y* misalignment.**

***Index Terms*—Capacitive power transfer (CPT), electric field emission, equivalent circuit model, six-plate coupler.**

Manuscript received September 23, 2016; accepted January 24, 2017. Date of publication February 2, 2017; date of current version October 6, 2017. This work was supported in part by the U.S. Department of Energy Graduate Automotive Technology Education Grant, in part by San Diego State University, in part by the University of Michigan, and in part by the Northwestern Polytechnical University. Recommended for publication by Associate Editor C. K. Tse.

H. Zhang is with the School of Automation, Northwestern Polytechnical University, Xi'an 710072, China, and also with the Department of Electrical and Computer Engineering,San Diego State University, San Diego, CA 92182 USA (e-mail: hzhang@mail.sdsu.edu).

F. Lu is with theDepartment of Electrical Engineering and Computer Science, University of Michigan, Ann Arbor, MI 48109 USA, and also with the Department of Electrical and Computer Engineering, San Diego State University, San Diego, CA 92182 USA (e-mail: feilu@umich.edu).

H. Hofmann is with theDepartment of Electrical Engineering and Computer Science, University of Michigan, Ann Arbor, MI 48109 USA (e-mail: hofmann@umich.edu).

W. Liu is with the School of Automation, Northwestern Polytechnical University, Xi'an 710072, China (e-mail: lwglll@nwpu.edu.cn).

C. C. Mi is with theDepartment of Electrical and Computer Engineering, San Diego State University, San Diego, CA 92182 USA (e-mail: mi@ieee.org).

Color versions of one or more of the figures in this paper are available online at http://ieeexplore.ieee.org.

Digital Object Identifier 10.1109/TPEL.2017.2662583

I. Introduction

CAPACITIVE power transfer (CPT) utilizes electric fields, instead of magnetic fields, to transfer power without galvanic contact [1], [2]. Despite parasitic displacement currents, electric fields do not generate significant eddy current loss in nearby metals, so the CPT system can be an attractive alternative to the traditional inductive power transfer (IPT) system [3], [4]. Furthermore, the CPT system uses metal plates as the capacitive coupler and eliminates ferrites, which reduces the system cost and weight.

However, application of CPT systems is currently limited by transfer distance and electric field emissions [5]. The coupling capacitance is determined by the plate area and distance. Since the power storage in a capacitor is calculated as $P = 0.5 f_{\mathrm{sw}} C V^2$, when the coupling capacitance is in the pF range, it requires either a high switching frequency or a high voltage to achieve high power transfer, which is difficult to realize in practice. Therefore, the short-distance CPT technology is mostly studied in previous research works [6]–[9].

One solution to increasing the transfer power and distance is to increase the voltage between the metal plates to establish a stronger electric field. Therefore, various compensation circuit topologies have been proposed to resonate with the capacitive coupler and produce high voltage. The double-sided LCLC [10], [11] compensation topology can increase the plate voltage to several kV, which resulted in a transfer power of 2.4 kW across a 150 mm air-gap for electric vehicle charging applications. It also has some variations, such as CLLC [12], LCL [13], [14], and LC [15] compensation. Moreover, *Z*-impedance compensation [16] and class-E amplifiers [17]–[20] can also help increase the plate voltage and achieve a high-efficiency CPT system. However, increasing the voltage may exceed the breakdown field of air between the plates, which can result in arcing. Also, the electric field emissions in the surrounding environment can exceed the safety requirements of the human body [21], which limits the maximum voltage for given gap distances.

One solution to reducing electric field emissions without reducing the plate voltage is to optimize the structure of the capacitive coupler. The external field cancellation method, which drives the adjacent metal plates with 180° phase difference to limit field emissions, is a good candidate, but it has special requirements on the control algorithm [22], [23]. Another can-

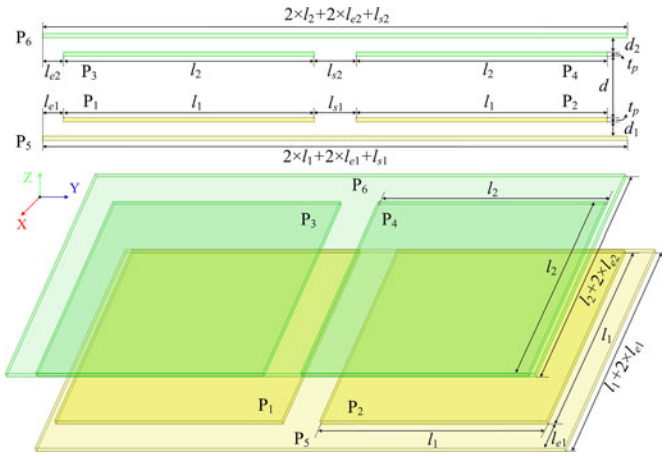

Fig. 1. Structure and dimensions of a six-plate coupler.

didate is the combination of a four-plate horizontal [10] and vertical [13] structure, which results in a six-plate capacitive coupler topology [24]. The two extra plates are large enough to cover the internal four plates. The external plates can provide coupling capacitors to simplify the compensation circuit. More importantly, they can also be used as electric field shields to reduce field emissions.

This paper will provide an equivalent circuit model of the six-plate coupler topology, which is then used to analyze the CPT system working principle and provide design circuit parameters. Similar to the four-plate vertical structure, the double-sided LCL compensation circuit is used to resonate with the six-plate coupler. Finite element analysis (FEA) by Maxwell compares the electric field emissions of the six-plate coupler to the four-plate horizontal and vertical couplers, and shows that the six-plate coupler achieves electric field shielding and therefore expands the safety area. Finally, a 1.97 kW CPT prototype is designed and implemented to validate the proposed six-plate coupler.

II. Six-Plate Capacitive Coupler and Its Circuit Model

A. Plate Structure

The six-plate capacitive coupler structure is shown in Fig. 1. Plates P_1, P_2, and P_5 are placed at the primary (transmitter) side, and P_3, P_4, and P_6 are at the secondary (receiver) side. P_1, P_2, P_3, and P_4 work as the power transfer plates. P_5 and P_6 work as the shielding plates, and they are larger than the other plates to provide better shielding of the electric fields. The dimensions of the six-plate coupler are also shown in Fig. 1. The definitions of the dimensions are described in Table I.

B. Full-Capacitor Model of Six-Plate Coupler

In the six-plate coupler, every two plates are capacitively coupled, which results in 15 coupling capacitors in total. Fig. 2 shows all the coupling capacitances between plates.

The capacitors C_{15} and C_{25} dominate the self-capacitance of the primary side, and the capacitors C_{36} and C_{46} dominate the self-capacitance of the secondary side. Since the two

TABLE I
Parameters Describing Six-Plate Structure

Parameter	Description	Parameter	Description
l_1	Primary plate length	l_2	Secondary plate length
l_{s1}	Primary plate separation	l_{s2}	Secondary plate separation
l_{e1}	Primary shielding edge	l_{e2}	Secondary shielding edge
d_1	Primary gap distance	d_2	Secondary gap distance
d	Primary–secondary gap	t_p	Plate thickness

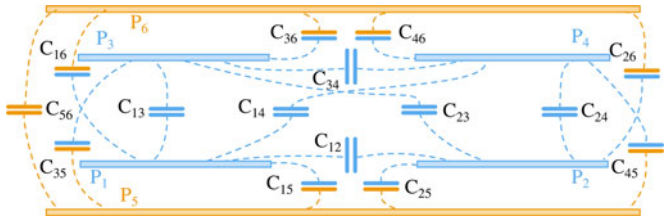

Fig. 2. Coupling capacitors between plates.

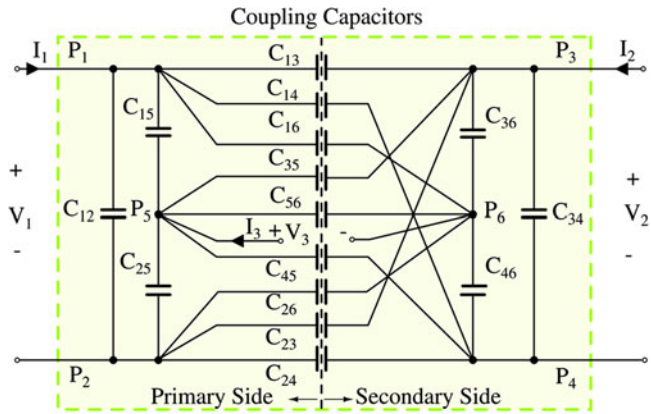

Fig. 3. Full-capacitor model of a six-plate coupler.

pairs of plates, $\mathrm{P}_1--\mathrm{P}_3$ and $\mathrm{P}_2--\mathrm{P}_4$, are the main power transfer plates, the capacitors C_{13} and C_{24} dominate the mutual capacitance between the primary and secondary sides. Other capacitors, such as C_{14}, C_{23}, etc., also affect the self and mutual capacitances.

Considering the all the couplings, the full-capacitor model of the coupler is shown in Fig. 3, in which V_1 and V_2 are the voltages at the primary and secondary sides, respectively. The voltage V_3 and current I_3 are imaginary external excitations between plates P_5 aand P_6, which are used to simplfy the circuit analysis. In real application $I_3 = 0$. Compared to the 4-plate model in [13], the 6-plate model is very complex. It is, therefore, useful to acquire an equivalent but simplified circuit model to help design the corresponding resonant circuit. In this paper, the full-capacitor model is first simplified as a three-port equivalent model and then a two-port model.

C. Three-Port Model of Six-Plate Coupler

A three-port network can be used to represent the equivalent circuit model of the six-plate coupler as shown in Fig. 4. Plates P_1 and P_2 are connected to the primary side circuit, and form

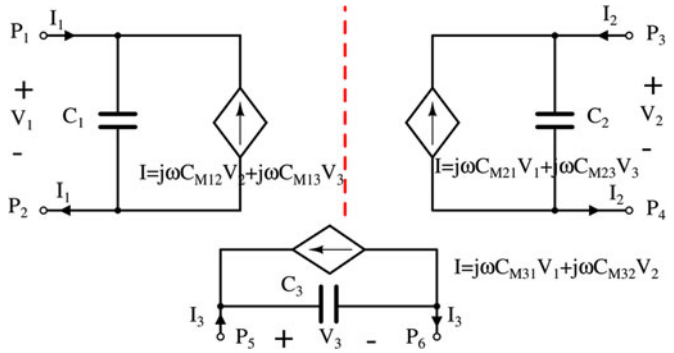

Fig. 4. Three-port behavior source model of a six-plate coupler.

the first port. Plates P_3 and P_4 are connected to the secondary side circuit and form the second port. Plates P_5 and P_6 form the third port, which is used to simplify analysis. The terminal voltages and currents of the three ports are represented as V_1, I_1, V_2, I_2, V_3, and I_3. The relationships between the variables are expressed as follows:

$$\begin{cases} I_1 = j\omega C_1 V_1 - j\omega C_{M12} V_2 - j\omega C_{M13} V_3 \\ I_2 = -j\omega C_{M21} V_1 + j\omega C_2 V_2 - j\omega C_{M23} V_3 \\ I_3 = -j\omega C_{M31} V_1 - j\omega C_{M32} V_2 + j\omega C_3 V_3 \end{cases} \tag{1}$$

where C_1, C_2, and C_3 are the self-capacitances at each of the three ports, C_{M12}, C_{M13}, C_{M21}, C_{M23}, C_{M31}, and C_{M32} are the mutual capacitances, and $\omega = 2\pi f_{\mathrm{sw}}$, where f_{sw} is the switching frequency. Using energy arguments, it can be shown that $C_{M12} = C_{M21}$, $C_{M13} = C_{M31}$, and $C_{M23} = C_{M32}$.

It is necessary to determine the relationships between the parameters in the full-capacitor model and the three-port model. The self-capacitances are calculated first, followed by the mutual capacitances. The self-capacitance C_1 is used as an example. According to (1), C_1 is determined as follows:

$$C_1 = \left.\frac{I_1}{j\omega V_1}\right|_{V_2 = V_3 = 0}. \tag{2}$$

Fig. 5 shows the process to simplify the circuit to get the equivalent model. When V_2 and V_3 are short-circuited, the full-capacitor model is shown in Fig. 5(a). I_1, I_2, and I_3 represent the currents induced by V_1 at the three ports. Since P_5 and P_6 are short-circuited, the capacitors can be combined together as shown in Fig. 5(b). It needs to be emphasized that the simplification from Fig. 5(a) to (b) does not affect the current I_2. To calculate the self-capacitance, the circuit is further simplified, as shown in Fig. 5(c). All the capacitors related to P_3, P_4, P_5, and P_6 are then combined together, as follows:

$$\begin{cases} C_{a1} = C_{13} + C_{14} \\ C_{b1} = C_{23} + C_{24} \\ C_{c1} = C_{15} + C_{16} \\ C_{d1} = C_{25} + C_{26} \\ C_{e1} = C_{35} + C_{36} + C_{45} + C_{46} \end{cases}. \tag{3}$$

The plate nodal voltages are defined as V_{P1}, V_{P2}, V_{P3}, and V_{P5}. P_2 is defined as the reference node, which means $V_{P2} = 0$. The Kirchhoff's current equations of the four nodes in Fig. 5(c)

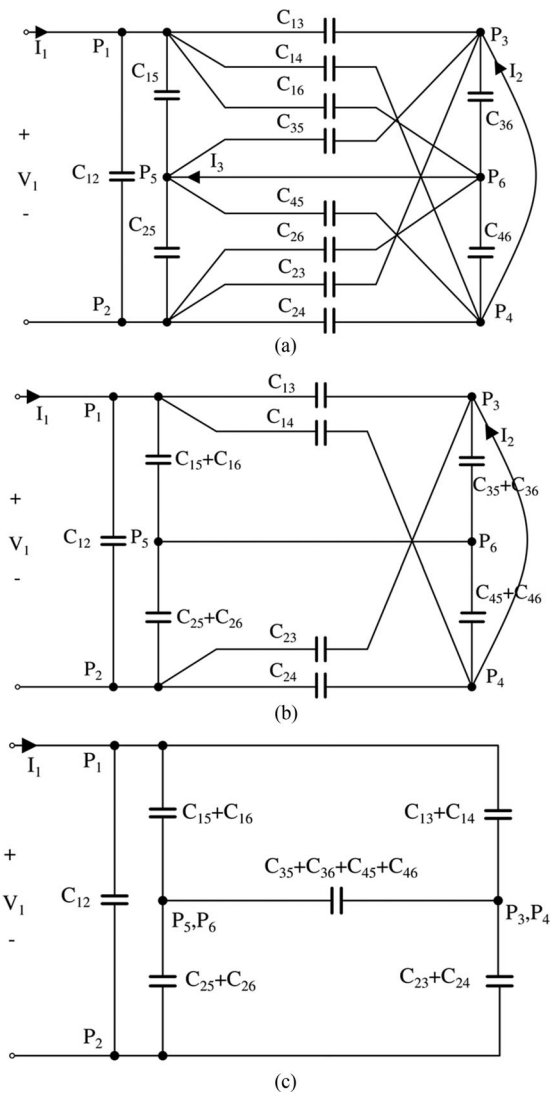

Fig. 5. Simplification process of capacitor model when $V_2 = V_3 = 0$. (a) Full-capacitor model, (b) combine parallel capacitors, and (c) further combine capacitors.

are expressed as

$$\begin{cases} (C_{12} + C_{a1} + C_{c1}) \cdot V_{P1} - C_{a1} V_{P3} - C_{c1} V_{P5} = I_1/(j\omega) \\ C_{12} V_{P1} + C_{b1} V_{P3} + C_{d1} V_{P5} = I_1/(j\omega) \\ (C_{a1} + C_{b1} + C_{e1}) \cdot V_{P3} - C_{a1} V_{P1} - C_{e1} V_{P5} = 0 \\ (C_{c1} + C_{d1} + C_{e1}) \cdot V_{P3} - C_{c1} V_{P1} - C_{e1} V_{P3} = 0 \end{cases}. \tag{4}$$

According to (4), V_{P3} and V_{P5} are expressed as

$$V_{P3} = V_{P4} = \frac{[C_{e1}(C_{a1} + C_{c1}) + C_{a1}(C_{c1} + C_{d1})] \cdot V_1}{C_{e1}(C_{a1} + C_{b1} + C_{c1} + C_{d1}) + (C_{a1} + C_{b1})(C_{c1} + C_{d1})}$$

$$V_{P5} = V_{P6} = \frac{[C_{e1}(C_{a1} + C_{c1}) + C_{c1}(C_{a1} + C_{b1})] \cdot V_1}{C_{e1}(C_{a1} + C_{b1} + C_{c1} + C_{d1}) + (C_{a1} + C_{b1})(C_{c1} + C_{d1})}. \tag{5}$$

To simplify analysis, capacitors C_{01} and C_T are defined as

$$C_{01} = \frac{C_{e1}(C_{a1}+C_{c1})(C_{b1}+C_{d1})}{C_{T1}} + \frac{C_{a1}C_{b1}(C_{c1}+C_{d1})+C_{c1}C_{d1}(C_{a1}+C_{b1})}{C_{T1}}$$
$$C_{T1} = C_{e1}(C_{a1}+C_{b1}+C_{c1}+C_{d1}) + (C_{a1}+C_{b1})\cdot(C_{c1}+C_{d1}). \quad (6)$$

The self-capacitance C_1 is then determined to be

$$C_1 = C_{12} + C_{01}. \quad (7)$$

After the self-capacitance C_1 is determined, the mutual capacitance C_{M12} can also be acquired with $V_2 = V_3 = 0$. From the second equation of (1), C_{M12} can be calculated as

$$C_{M12} = \left.\frac{I_2}{-j\omega V_1}\right|_{V_2=V_3=0}. \quad (8)$$

Fig. 5(b) can be used to calculate C_{M12}. At node P_4, the current I_2 can be expressed as

$$\frac{I_2}{j\omega} = -(C_{14}+C_{24}+C_{45}+C_{46})V_{P4} + C_{14}V_{P1} + (C_{45}+C_{46})V_{P6}. \quad (9)$$

By substituting (5) into (9), the mutual capacitance is expressed as

$$C_{M12} = \frac{C_{e1}(C_{24}C_{c1}-C_{14}C_{d1})+(C_{45}+C_{46})(C_{a1}C_{d1}-C_{b1}C_{c1})}{C_{T1}} + \frac{(C_{13}C_{24}-C_{14}C_{23})(C_{c1}+C_{d1}+C_{e1})}{C_{T1}}. \quad (10)$$

Therefore, when V_2 and V_3 are short-circuited, the self-capacitance C_1 is expressed in (7), and the mutual capacitance C_{M12} is expressed in (10). The parameters C_1 and C_{M12} are shown in the first column in Table II.

Following similar procedures, the parameters C_2 and C_{M23} are determined with V_1 and V_3 short-circuited, and shown in the second column in Table II. The parameters C_3 and C_{M13} are acquired with V_1 and V_2 short-circuited, and shown in the third column in Table II. In conclusion, all the equivalent self- and mutual-capacitances of the six-plate coupler are summarized in Table II. It can be further proved that $C_{T1} = C_{T2} = C_{T3}$, so they can be represented by C_T. It shows that equivalent capacitances depend on the couplings between plates.

D. Two-Port Model of Six-Plate Coupler

When the six-plate coupler is connected into a circuit, only P_1, P_2, P_3, and P_4 are directly connected and P_5 and P_6 are floating. This means there is no external voltage or current source connected to P_5 and P_6, and hence $I_3 = 0$. The three-port circuit model is then further simplified into an equivalent two-port model shown in Fig. 6.

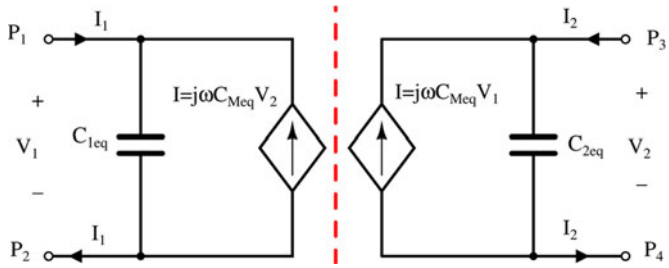

Fig. 6. Two-port equivalent model of six-plate coupler.

The equivalent 2-port parameters are calculated from (1) with $I_3 = 0$, which results in

$$\begin{cases} I_1 = j\omega\left(C_1 - \dfrac{C_{M13}^2}{C_3}\right)\cdot V_1 \\ \qquad -j\omega\left(C_{M12} + \dfrac{C_{M13}C_{M23}}{C_3}\right)\cdot V_2 \\ I_2 = -j\omega\left(C_{M12} + \dfrac{C_{M13}C_{M23}}{C_3}\right)\cdot V_1 \\ \qquad +j\omega\left(C_2 - \dfrac{C_{M23}^2}{C_3}\right)\cdot V_2 \end{cases}. \quad (11)$$

Therefore, the equivalent 2-port parameters are expressed as

$$\begin{cases} C_{1\mathrm{eq}} = C_1 - \dfrac{C_{M13}^2}{C_3} \\ C_{2\mathrm{eq}} = C_2 - \dfrac{C_{M23}^2}{C_3} \\ C_{M\mathrm{eq}} = C_{M12} + \dfrac{C_{M13}C_{M23}}{C_3} \end{cases}. \quad (12)$$

III. Example of Large Air-Gap CPT System With Six-Plate Coupler

A. Coupler Dimension Design

To simplify the design process, the transmitter and receiver plates are symmetric in this case. The primary and secondary plate lengths are therefore $l_1 = l_2 = 610\,\mathrm{mm}$, the plate separations are $l_{s1} = l_{s2} = 100\,\mathrm{mm}$, and the shielding plate edge lengths are $l_{e1} = l_{e2} = 50\,\mathrm{mm}$. The primary–secondary gap is 150 mm, aiming at electric vehicle charging applications. The influence of plate thickness ($t_p = 2\,\mathrm{mm}$) on the couplings can be neglected. The primary and secondary plate distances are also the same, which means $d_1 = d_2$. Therefore, d_1 is the only parameter that needs to be designed.

ANSYS Maxwell is used to perform FEA of the six-plate coupler. It provides the 15 coupling capacitances between every two plates. Table II is then used to calculate the equivalent capacitances. Due to the symmetry of the coupler, $C_1 = C_2$. When the transmitter and receiver are well-aligned and d_1 varies, C_1, C_3, and C_{M12} are shown in Fig. 7. Since C_{M13} and C_{M23} are smaller than 0.1 pF, they are neglected.

The self-capacitances C_1 and C_3 decrease with increasing d_1, and the mutual capacitance C_{M12} increases slightly with d_1. A larger C_{M12} means higher transfer power; however, a

TABLE II
EQUIVALENT SELF- AND MUTUAL CAPACITANCES OF SIX-PLATE COUPLER

V_2=V_3=0	V_1=V_3=0	V_1=V_2=0
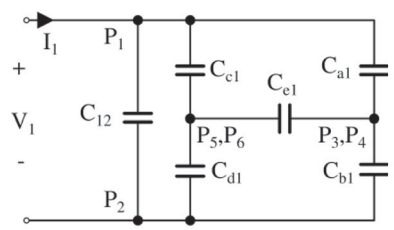	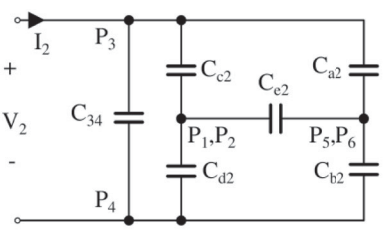	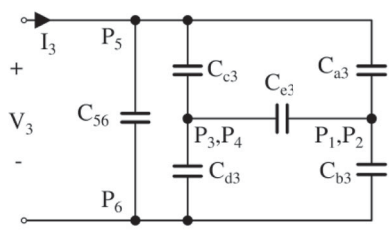
$\begin{cases} C_{a1} = C_{13} + C_{14} \\ C_{b1} = C_{23} + C_{24} \\ C_{c1} = C_{15} + C_{16} \\ C_{d1} = C_{25} + C_{26} \\ C_{e1} = C_{35} + C_{36} + C_{45} + C_{46} \end{cases}$	$\begin{cases} C_{a2} = C_{35} + C_{36} \\ C_{b2} = C_{45} + C_{46} \\ C_{c2} = C_{13} + C_{23} \\ C_{d2} = C_{14} + C_{24} \\ C_{e2} = C_{15} + C_{16} + C_{25} + C_{26} \end{cases}$	$\begin{cases} C_{a3} = C_{15} + C_{25} \\ C_{b3} = C_{16} + C_{26} \\ C_{c3} = C_{35} + C_{45} \\ C_{d3} = C_{36} + C_{46} \\ C_{e3} = C_{13} + C_{14} + C_{23} + C_{24} \end{cases}$
$C_1 = C_{12} + C_{01}$	$C_2 = C_{34} + C_{02}$	$C_3 = C_{56} + C_{03}$
$C_{M12} = \frac{C_{e1}(C_{24}C_{c1} - C_{14}C_{d1})}{C_T} + \frac{(C_{45} + C_{46})(C_{a1}C_{d1} - C_{b1}C_{c1})}{C_T} + \frac{(C_{13}C_{24} - C_{14}C_{23})(C_{c1} + C_{d1} + C_{e1})}{C_T}$	$C_{M23} = \frac{C_{e2}(C_{46}C_{c2} - C_{36}C_{d2})}{C_T} + \frac{(C_{16} + C_{26})(C_{a2}C_{d2} - C_{b2}C_{c2})}{C_T} + \frac{(C_{35}C_{46} - C_{36}C_{45})(C_{c2} + C_{d2} + C_{e2})}{C_T}$	$C_{M13} = \frac{C_{e3}(C_{26}C_{c3} - C_{25}C_{d3})}{C_T} + \frac{(C_{24} + C_{23})(C_{a3}C_{d3} - C_{b3}C_{c3})}{C_T} + \frac{(C_{15}C_{26} - C_{16}C_{25})(C_{c3} + C_{d3} + C_{e3})}{C_T}$
$\begin{cases} C_T = C_{ei}(C_{ai} + C_{bi} + C_{ci} + C_{di}) + (C_{ai} + C_{bi}) \cdot (C_{ci} + C_{di}) \\ C_{0i} = \frac{C_{ei}(C_{ai} + C_{ci})(C_{bi} + C_{di}) + C_{ai}C_{bi}(C_{ci} + C_{di}) + C_{ci}C_{di}(C_{ai} + C_{bi})}{C_T} \end{cases}$, i=1, 2, 3		

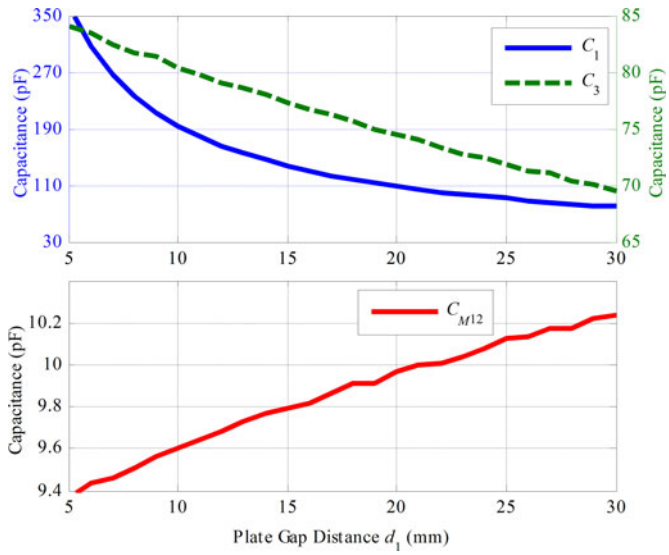

Fig. 7. Maxwell-simulated equivalent capacitances at different d_1.

low self-capacitance requires a large resonant inductor, which is difficult to realize. Therefore, d_1 is set to be 19 mm in this case, which results in the Maxwell-simulated original and equivalent capacitances as shown in Table III. The differences between C_{15}, C_{25}, C_{36}, and C_{46} are due to the calculation tolerance of the Maxwell solver.

TABLE III
MAXWELL-SIMULATED AND EQUIVALENT CAPACITANCES WHEN WELL-ALIGNED AND d_1 = 19 MM

	P_1	P_2	P_3	P_4	P_5	P_6
P_1		0.77pF	20.38pF	0.56pF	200.48pF	4.42pF
P_2	0.77pF		0.52pF	20.35pF	197.75pF	4.26pF
P_3	20.38pF	0.52pF		0.77pF	4.27pF	198.35pF
P_4	0.56pF	20.35pF	0.77pF		4.41pF	200.64pF
P_5	200.48pF	197.75pF	4.27pF	4.41pF		26.11pF
P_6	4.42pF	4.26pF	198.35pF	200.64pF	26.11pF	
	C_1 = 112.94pF		C_{M12} = 9.91pF		C_{M13} = 0.04pF	
	C_{M21} = 9.91pF		C_2 = 112.94pF		C_{M23} = 0.05pF	
	C_{M31} = 0.04pF		C_{M32} = 0.05pF		C_3 = 74.90pF	

With the designed dimensions, the misalignment ability of the coupler is analyzed in Maxwell, and the simulated capacitances are shown in Figs. 8 and 9. The *X* and *Y* directions are defined in Fig. 1.

Fig. 8 shows the equivalent capacitances C_3 and C_{M12} with *X*-direction misalignment. Compared to the well-aligned case, the variations of the other capacitances are too small to be neglected. This indicates that C_3 decreases by 12.2% and C_{M12} decreases by 36.7% when the *X* misalignment is 300 mm.

Fig. 9 shows the equivalent capacitances C_3, C_{M12}, C_{M13}, and C_{M23} with *Y*-direction misalignment. The variations of the other capacitances are also neglected. It indicates that C_3 decreases by 6.7% and C_{M12} decreases by 54.4% when the *Y*

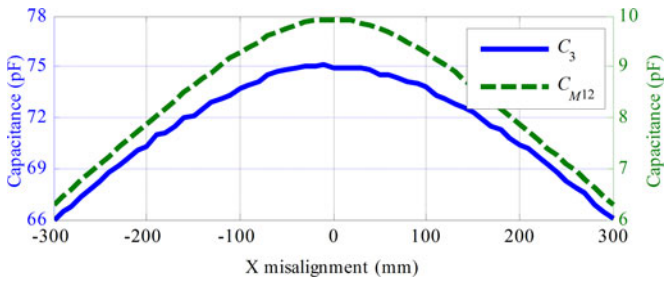

Fig. 8. Maxwell-simulated capacitances at *X* misalignment conditions.

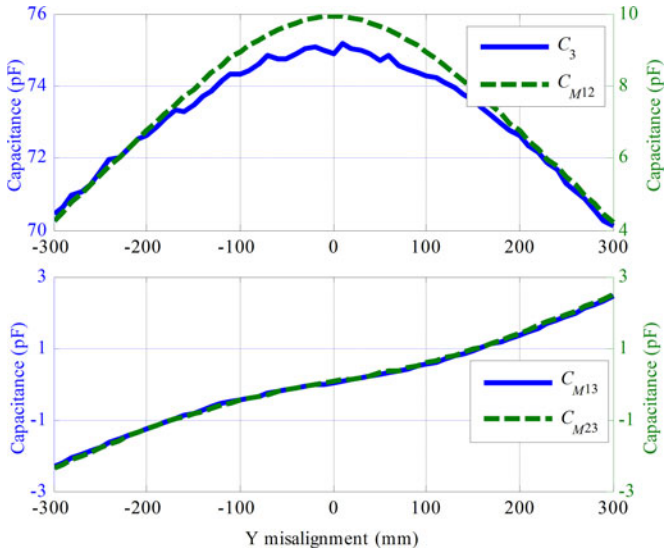

Fig. 9. Maxwell-simulated capacitances at *Y* misalignment conditions.

misalignment is 300 mm. It also shows that the mutual capacitances $C_{M13} = C_{M23}$ in the *Y* misalignment case, and their absolute value is 2.4 pF at 300 mm *Y* misalignment. The negative value of capacitance indicates that the direction of induced current is opposite the predefined positive direction.

B. LCL Compensation Topology

The six-plate coupler can eliminate an external parallel capacitor in the previous LCLC topology [10], which results in an LCL compensation and reduces system cost. The circuit topology is shown in Fig. 10. A full-bridge inverter is used to inject ac excitation, and a full-bridge rectifier provides dc current to the load. When the coupler is represented by the 2-port model, the equivalent circuit of the CPT system is shown in Fig. 11.

The output power of the CPT system [13] is expressed as

$$P_{\text{out}} = \frac{\omega \cdot C_{M\text{eq}} \cdot C_{f1}C_{f2}}{(1-k_C^2)\cdot C_{1\text{eq}}C_{2\text{eq}}} \cdot |V_{\text{in}}| \cdot |V_{\text{out}}| \tag{13}$$

where C_{f1} and C_{f2} are the compensation capacitors, V_{in} and V_{out} are rms values of the ac input and output voltages to the resonant tank, and k_C is the capacitive coupling coefficient,

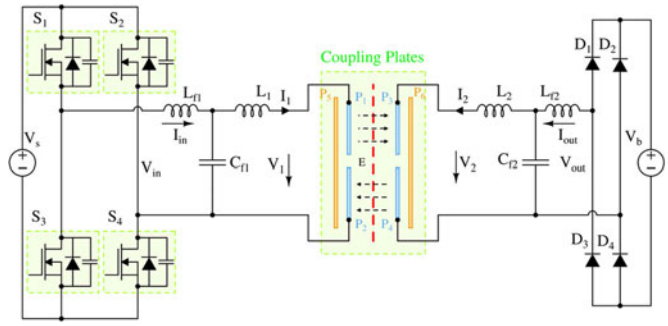

Fig. 10. Circuit topology of an LCL-compensated six-plate CPT system.

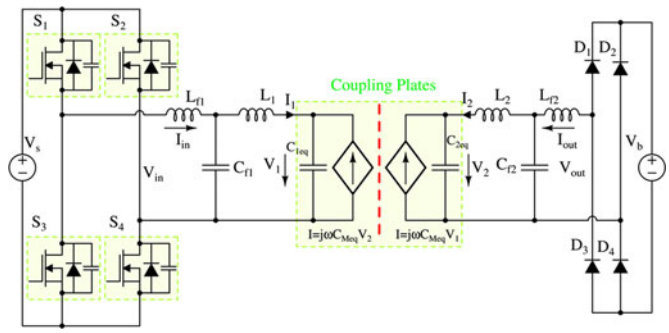

Fig. 11. Equivalent circuit of an LCL compensated six-plate CPT system.

TABLE IV
SYSTEM SPECIFICATIONS AND CIRCUIT PARAMETERS

Parameter	Design Value	Parameter	Design Value
V_s	270 V	V_b	270 V
l_1 (l_2)	610 mm	l_{s1} (l_{s2})	50 mm
l_{e1} (l_{e2})	50 mm	d_1 (d_2)	19 mm
t_p	2 mm	d	150 mm
f_{sw}	1 MHz	$C_{M\text{eq}}$	9.91 pF
L_{f1}	9.21 μH	L_{f2}	9.21 μH
C_{f1}	2.75 nF	C_{f2}	2.75 nF
L_1	235.3 μH	L_2	244.7 μH
$C_{1\text{eq}}$	112.9 pF	$C_{2\text{eq}}$	112.9 pF

which is defined as follows:

$$k_C = \frac{C_{M\text{eq}}}{\sqrt{C_{1\text{eq}} \cdot C_{2\text{eq}}}}. \tag{14}$$

The parameters should satisfy the following resonant relationships:

$$\begin{aligned} &\omega = 2\pi f_{\text{sw}} = 1/\sqrt{L_{f1}C_{f1}} = 1/\sqrt{L_{f2}C_{f2}}, \\ &L_1 = 1/(\omega^2 C_{f1}) + 1/(\omega^2 C_{1\text{eq}}), L_2 \\ &= 1/(\omega^2 C_{f2}) + 1/(\omega^2 C_{2\text{eq}}). \end{aligned} \tag{15}$$

C. 2.0 kW CPT System Parameter Design

According to (13)–(15), a 2.0 kW CPT system is designed with the six-plate coupler. The system specifications and circuit parameters are shown in Table IV.

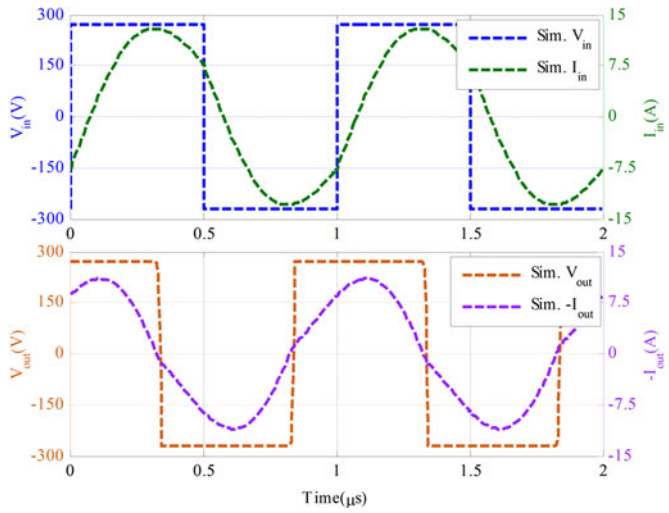

Fig. 12. LTspice-simulated input and output waveforms of the designed system.

The input and output dc voltages are both set at 270 V to achieve a 2.0 kW output. The switching frequency is 1 MHz. Most of the parameters are symmetric from the primary to secondary side, except that L_2 is slightly larger than L_1 to provide a soft-switching condition to the MOSFETs of the input inverter.

The circuit performance is simulated in LTspice, and the waveforms are shown in Fig. 12. It is seen that the input voltage and current are almost in phase, which limits the reactive power circulating in the circuit and therefore increases the system efficiency. The output voltage and current are also in phase on the rectifier side.

IV. Electric Field Shielding of Six-Plate Coupler

A. Voltage Between Plates

The voltages between the plates determine the electric field emissions to the surrounding environment. The voltages V_1 and V_2 are the external inputs to the six-plate coupler, and are also the voltage between plates P_1 and P_2, and plates P_3 and P_4 [13]. In Fig. 11, the voltages can be calculated as

$$V_1 = \frac{C_{f1}\cdot V_{\text{in}}}{(1-k_C^2)\cdot C_{1\text{eq}}} + \frac{C_{M\text{eq}}C_{f2}\cdot V_{\text{out}}}{(1-k_C^2)\cdot C_{1\text{eq}}C_{2\text{eq}}}$$
$$V_2 = \frac{C_{M\text{eq}}C_{f1}\cdot V_{\text{in}}}{(1-k_C^2)\cdot C_{1\text{eq}}C_{2\text{eq}}} + \frac{C_{f2}\cdot V_{\text{out}}}{(1-k_C^2)\cdot C_{2\text{eq}}}. \quad (16)$$

According to (1) and $I_3 = 0$, the voltage stress between P_5 and P_6 is expressed as

$$V_3 = \frac{C_{M13}}{C_3}V_1 + \frac{C_{M23}}{C_3}V_2. \quad (17)$$

The coupler dimension design in Section III-A shows that C_{M13} and C_{M23} are zero in the well-aligned case, which means the voltage between P_5 and P_6 is zero. When there is 300 mm *X* or *Y* misalignment, there exist $C_{M13} \ll C_3$ and $C_{M23} \ll C_3$. Therefore, V_3 is limited, and the electric field emissions are reduced.

TABLE V
RMS Value of the Voltage Stresses Between Plates

Parameters	Well-aligned	300 mm *X* misalignment	300 mm *Y* misalignment
$\lvert V_{P1-P2}\rvert$	6.51 kV	6.47 kV	6.44 kV
$\lvert V_{P1-P3}\rvert$	4.18 kV	4.32 kV	4.40 kV
$\lvert V_{P1-P5}\rvert$	3.25 kV	3.26 kV	3.28 kV
$\lvert V_{P5-P6}\rvert$	0	0	0.34 kV

The voltage between plates on the same side should be limited to avoid potential arcing problems. Using (5) and similar analysis process in Section II-C, the voltage between plates P_1 and P_5 is calculated as

$$V_{P1-P5} = \frac{C_{e1}(C_{b1}+C_{d1})+C_{d1}(C_{a1}+C_{b1})}{C_T}\cdot V_1 + \frac{C_{a2}C_{d2}-C_{b2}C_{c2}}{C_T}\cdot V_2 - \frac{C_{e3}(C_{b3}+C_{d3})+C_{b3}(C_{c3}+C_{d3})}{C_T}\cdot V_3. \quad (18)$$

Similarly, the voltage between the other plates, such as V_{P2--P5}, V_{P3--P6}, V_{P4--P6}, V_{P1--P3}, etc., can also be calculated [13]. Due to the symmetry of the coupler and circuit parameters, $|V_{P1--P2}| = |V_{P3--P4}|$, $|V_{P1--P3}| = |V_{P2--P4}|$, and $|V_{P1--P5}| = |V_{P2--P5}| = |V_{P3--P6}| = |V_{P4--P6}|$. By substituting the values in Table IV, the voltages between plates are shown in Table V.

This shows that the voltage between plates P_5 and P_6 is limited to 0.34 kV in the misalignment case. Therefore, the electric field emissions are reduced. The voltage between P_1 and P_5 is 3.25 kV, and the distance between them is 19 mm. Since the breakdown voltage of dry air is about 3 kV/mm, there is no significant concern about arcing between plates.

B. Electric Field Shielding

The electric field emissions to the surrounding environment relate to the safety of the CPT technology in practical applications. In this design, a 2.0 kW six-plate CPT system has a power density of 1.95 kW/m^2. The electric field should be smaller than 614 V/mm at 1 MHz [21]. Maxwell is used to simulate the shielding effect of the six-plate coupler, as shown in Fig. 13.

In Fig. 13, there are charge excitations on P_1, P_2, P_3, and P_4. The two shielding plates P_5 and P_6 are floating, and there is no charge excitation on them. The primary shielding plate P_5 is set as the voltage reference, and the voltages of the other plates achieve the values listed in Table V. The region that has an electric field strength higher than 614 V/m is illustrated in red. The maximum field strength between the transmitter and receiver plates is 27 kV/m, and the maximum field strength between the same side power and shielding plates can reach 170 kV/m. Due to the shielding effect of P_5 and P_6, the electric field is dramatically reduced above and below the coupler. There is only a small field from the air-gap leaking out to the surroundings, and it decreases quickly with distance. The safety range is about 0.1 m away from this coupler.

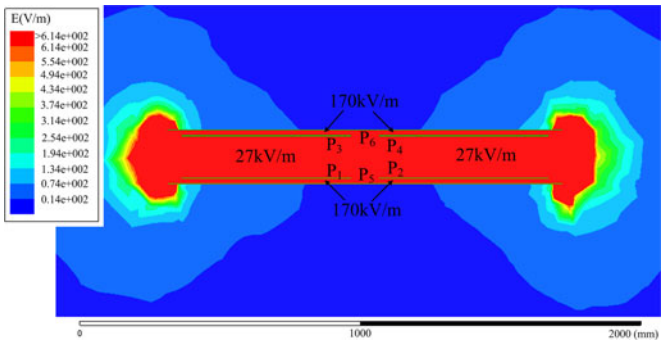

Fig. 13. Maxwell-simulated shielding effect of a six-plate coupler under well-aligned condition.

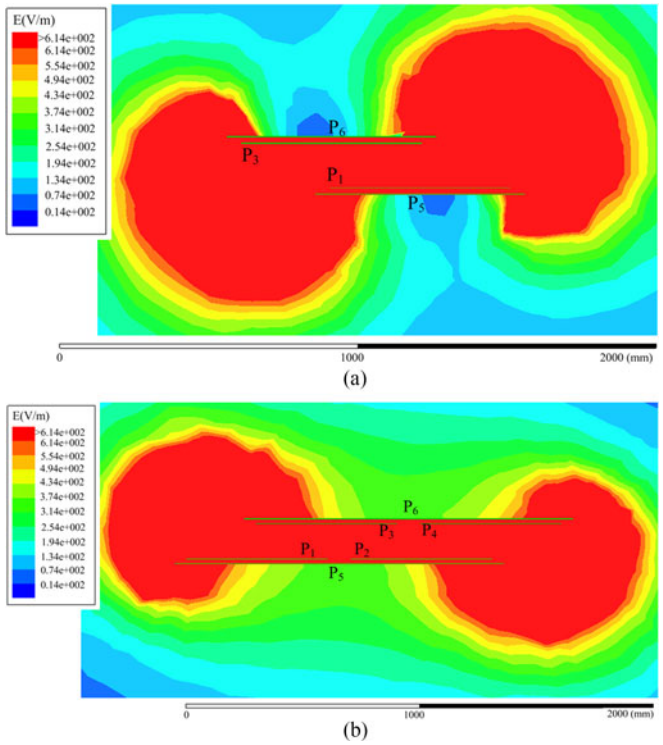

Fig. 14. Maxwell-simulated electric field emission of six-plate coupler at 300 mm misalignment condition (a) *X* misalignment and (b) *Y* misalignment.

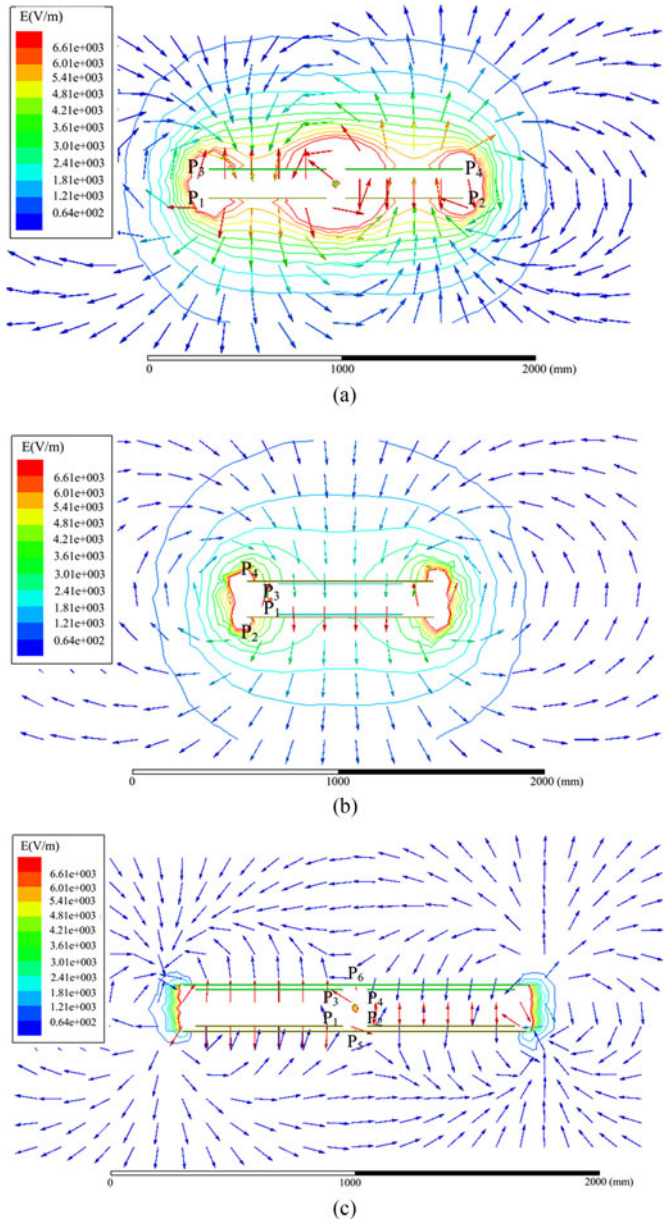

Fig. 15. Maxwell-simulated electric vector distribution of different couplers. (a) Four-plate horizontal coupler, (b) four-plate vertical coupler, and (c) six-plate coupler.

Fig. 14 shows the electric field emission when there is 300 mm *X*- and *Y*-direction misalignment. Since the plates P_5 and P_6 cannot provide as good of a shielding effect with misalignment, the leakage field is increased. The safety range is 0.4 m from the coupler when there is misalignment.

C. Comparison With Four-Plate Coupler

According to [10] and [13], four plates are sufficient to form a capacitive coupler, and can be horizontally or vertically arranged. The four-plate horizontal coupler is very basic. It can resonate with an LCLC compensation circuit. In a 2.4 kW CPT system with a power density of 2.29 kW/m^2, the safety range is about 0.6 m away from the right and left of the coupler, and 0.9 m away from the top and bottom of the coupler [10].

The four-plate vertical structure is more compact, where two of the plates are smaller and vertically arranged with the other two plates. It resonates with an LCL compensation circuit. In a 1.9 kW CPT system with a power density of 2.25 kW/m^2, the safety range is about 1.0 m away from the coupler [13].

Compared to the four-plate structure, the six-plate coupler can significantly reduce the electric field emissions to the surroundings. At similar power levels, the safety range of the six-plate coupler is increased. This phenomenon can be explained by the electric field vector (E vector) distribution. The vector direction is determined by the voltage difference between plates. The E vectors of the four-plate horizontal, four-plate vertical, and six-plate systems are shown in Fig. 15(a), (b), and (c), respectively.

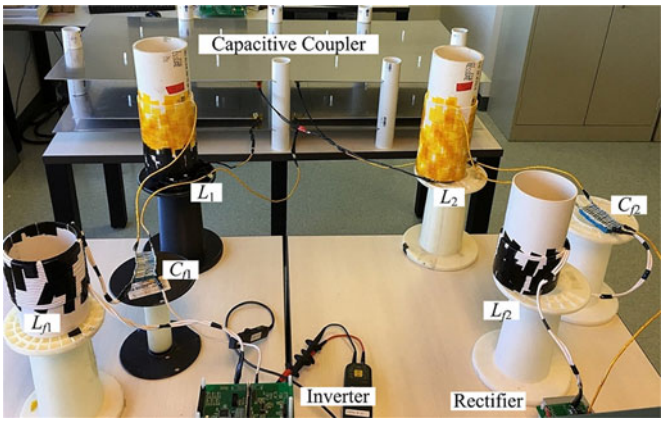

Fig. 16. Experiment prototype of a 2.0 kW CPT system with a six-plate coupler.

In Fig. 15(a), there is a large voltage difference between every pair of plates [10]. Therefore, the E vector indicates that the electric flux goes from one plate to the other. Since the air-gap between the plates is large, the leakage flux causes significant electric field emissions. In Fig. 15(b), there is a voltage difference between P_2 and P_4 [13], so the electric flux goes from P_2 to P_4, which generates electric field emissions. In Fig. 15(c), there is no voltage difference between P_5 and P_6, so there is no electric flux going directly between them. Because P_6 is floating and covers P_3 and P_4, it limits the electric flux between P_3 and P_4 to below P_6. Symmetrically, the leakage flux to the bottom of P_5 is also limited. Therefore, the plates P_5 and P_6 can act as electric field shielding.

V. Experimental Results

A. Experimental Setup

Using the designed six-plate coupler and compensation parameters in Table IV, a 2.0 kW CPT system is implemented as shown in Fig. 16. The coupler is made with 2 mm thickness aluminum plates, and PVC tubes are used to hold the coupler plates in place. Ceramic spacers are used between the same side plates to provide insulation. The distance between the transmitter and receiver is 150 mm.

Since the switching frequency is 1 MHz, silicon carbide (SiC) MOSFETs (C2M0080120D) are used in the inverter, and SiC diodes (IDW30G65C) are used in the rectifier. To reduce the power losses induced by the skin effect, 3000-strands AWG 46 Litz-wire is used in the windings of the compensation inductors. The inductors have air cores to further eliminate magnetic losses. Furthermore, high-frequency and low-loss thin-film capacitors are used for the compensation capacitors.

B. Well-Aligned Experiment

When the transmitter and receiver are well-aligned, the experimental results of six-plate CPT system are shown in Fig. 17. In Fig. 17(a), when the input and output dc voltages are both 270 V, the system output power is 1.97 kW, and the dc–dc efficiency from the dc source to electronic dc load is 91.6%. In Fig. 17(b), the input voltage and current are almost in phase

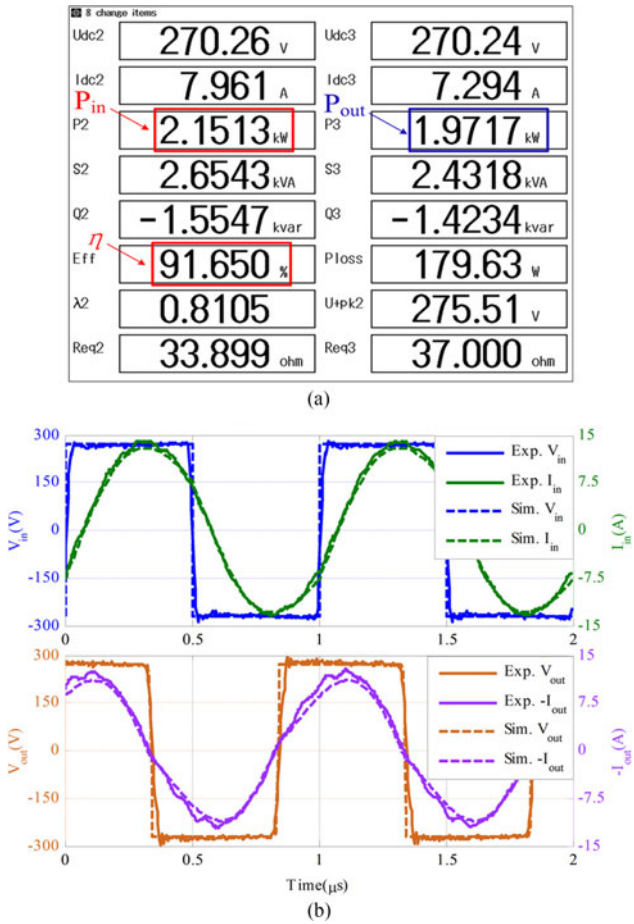

Fig. 17. Experimental results of six-plate CPT system at well-aligned case. (a) System power and (b) input and output waveforms.

with each other, which limits the reactive power circulating in the resonant circuit. The cut-off current at the switching transient is about 6 A, which helps the soft-switching of MOSFETs in the inverter. The experimental waveforms are extracted from the oscilloscope, which agree well with the LTspice simulation in Fig. 12, which validate the proposed CPT system.

In full-power condition, Fig. 17(a) shows that the total power loss is 179.6 W. Using a power loss model for each component [25], the power losses can be estimated in inductors, capacitors, MOSFETs, and diodes. This suggests that the remaining losses are in the metal plates. Therefore, the loss distribution among the circuit components is estimated as shown in Fig. 18. It indicates that the six-plate coupler dissipates 34% of the total loss. Since the plate area is large, there is not any significant temperature rise on the plates.

The relationship between output power and dc–dc efficiency is shown in Fig. 19. The system dc–dc efficiency increases with the output power. After the output power reaches 400 W, the dc–dc efficiency is maintained higher than 91%.

C. Misalignment Experiment

The misalignment experiment is performed in the *X* and *Y* directions, and the results are shown in Fig. 20. When the *X* misalignment is 300 mm, the output power decreases to 65% of the well-aligned value, and the dc–dc efficiency drops from

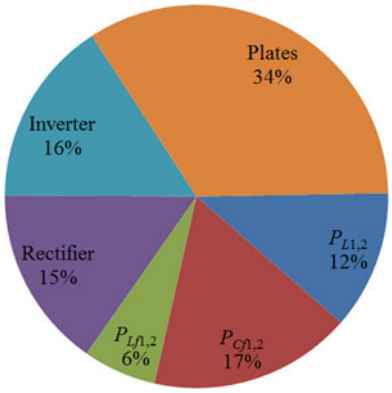

Fig. 18. Estimated power loss distribution in a six-plate CPT system.

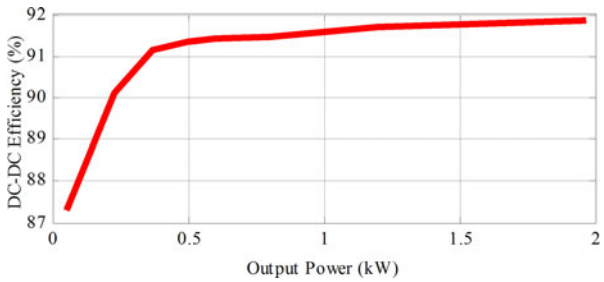

Fig. 19. Experimental output power and dc–dc efficiency in well-aligned case.

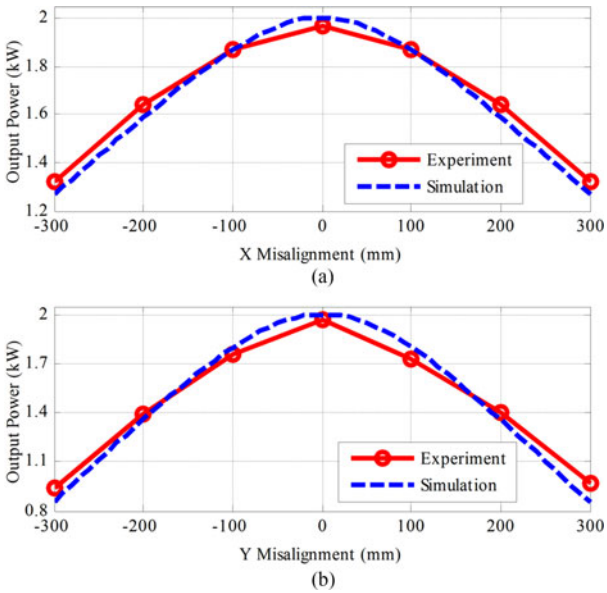

Fig. 20. Experimental and simulated misalignments of six-plate CPT system. (a) *X* misalignment and (b) *Y* misalignment.

91.6% to 91.0%. When the *Y* misalignment is 300 mm, the output power decreases to 49% of the well-aligned value and the dc–dc efficiency drops to 89.2%. Therefore, the six-plate coupler has better misalignment ability in the *X* direction than the *Y* direction.

The misalignment ability is also simulated in LTspice, using the parameters in Figs. 8 and 9. The experiment results agree well with the simulations, which also proves the effectiveness of the six-plate coupler and validates the proposed circuit model of the previous analysis. In future research, the misalignment performance will be improved by the coupler structure design.

VI. Conclusion

This paper proposes a six-plate coupler structure for a large-air-gap CPT system to reduce electric field emissions to the surroundings. Two large metal plates cover a four-plate horizontal coupler on top and bottom to provide shielding. Equivalent three-port and two-port behavior source models of the coupler are derived. The six-plate coupler can eliminate the external parallel capacitor in the previous LCLC topology, which results in the LCL compensation and reduces the system cost. A 2.0 kW CPT system is design and implemented with the six-plate coupler. It shows that the voltage between the shielding plates is limited, which contributes to the reduction of electric field emissions. FEA analysis by Maxwell shows that the safety range of the six-plate coupler is 0.1 m in the well-aligned case, and 0.4 m in the 300 mm *X* or *Y* misalignment case. Compared to the four-plate horizontal and vertical coupler, the safety area is significantly increased. A 2.0 kW CPT prototype with six-plate coupler is implemented, and experiment results show that the six-plate coupler achieves 1.97 kW power transfer with a dc–dc efficiency of 91.6% across an air-gap of 150 mm. In future research, the six-plate coupler structure will be studied in dynamic charging applications.

References

[1] J. Dai and D. C. Ludois, "Single active switch power electronics for kilowatt scale capacitive power transfer," *IEEE J. Emerg. Sel. Power Electron.*, vol. 3, no. 1, pp. 315–323, Mar. 2015.

[2] S. K. Mishra, R. Adda, S. Sekhar, A. Joshi, and A. K. Rathore, "Power transfer using portable surfaces in capacitively coupled power transfer technology," *IET Power Electron.*, vol. 9, no. 5, pp. 997–1008, 2016.

[3] C. Liu, A. P. Hu, and N. C. Nair, "Modelling and analysis of a capacitively coupled contactless power transfer system," *IET Power Electron.*, vol. 4, no. 7, pp. 808–815, 2011.

[4] D. Rozario, N. A. Azeez, and S. S. Williamson, "Analysis and design of coupling capacitors for contactless capacitive power transfer systems," in *Proc. IEEE Transp. Electr. Conf. Expo.*, 2016, pp. 1–7.

[5] J. Dai and D. Ludois, "A survey of wireless power transfer and a critical comparison of inductive and capacitive coupling for small gap applications," *IEEE Trans. Power Electron.*, vol. 30, no. 11, pp. 6017–6029, Nov. 2015.

[6] D. C. Ludois, J. K. Reed, and K. Hanson, "Capacitive power transfer for rotor field current in synchronous machines," *IEEE Trans. Power Electron.*, vol. 27, no. 11, pp. 4638–4645, Nov. 2012.

[7] K. H. Yi, "High frequency capacitive coupling wireless power transfer using glass dielectric layers," in *Proc. IEEE Wireless Power Transfer Conf.*, 2016, pp. 1–3. doi: 10.1109/WPT.2016.7498857.

[8] A. Sepahvand, A. Kumar, K. Afridi, and D. Maksimovic, "High power transfer density and high efficiency 100MHz capacitive wireless power transfer system," in *Proc. IEEE Workshop Control Model. Power Electron.*, 2015, pp. 1–4. doi: 10.1109/COMPEL.2015.7236492.

[9] C. K. Chang, G. G. Silva, A. Kumar, S. Pervaizz, and K. K. Afridi, "30W capacitive wireless power transfer system with 5.8pF coupling capacitance," in *Proc. IEEE Wireless Power Transfer Conf.*, 2015, pp. 1–4. doi: 10.1109/WPT.2015.7140184.

[10] F. Lu, H. Zhang, H. Hofmann, and C. Mi, "A double-sided LCLC-compensated capacitive power transfer system for electric vehicle charging," *IEEE Trans. Power Electron.*, vol. 30, no. 11, pp. 6011–6014, Nov. 2015.

[11] C. Mi, "High power capacitive power transfer for electric vehicle charging applications," in *Proc. Int. Conf. Power Electron. Syst. Appl.*, 2015, pp. 1–4.

[12] F. Lu, H. Zhang, H. Hofmann, and C. Mi, "A CLLC-compensated high power and large air-gap capacitive power transfer system for electric vehicle charging applications," in *Proc. IEEE Appl. Power Electr. Conf.*, 2016, pp. 1721–1725.
[13] H. Zhang, F. Lu, H. Hofmann, W. Liu, and C. Mi, "A four-plate compact capacitive coupler design and LCL-compensated topology for capacitive power transfer in electric vehicle charging application," *IEEE Trans. Power Electron.*, vol. 31, no. 12, pp. 8541–8551, Dec. 2016.
[14] M. P. Theodoridis, "Effective capacitive power transfer," *IEEE Trans. Power Electron.*, vol. 27, no. 12, pp. 4906–4913, Dec. 2012.
[15] F. Lu, H. Zhang, H. Hofmann, and C. Mi, "An inductive and capacitive combined wireless power transfer system with LC-compensated topology," *IEEE Trans. Power Electron.*, vol. 31, no. 12, pp. 8471–8482, Dec. 2016.
[16] L. Huang, A. P. Hu, A. K. Swain, and Y. Su, "Z-impedance compensation for wireless power transfer based on electric field," *IEEE Trans. Power Electron.*, vol. 31, no. 11, pp. 7556–7563, Nov. 2016.
[17] Y. Yusop, Z. Ghani, S. Saat, H. Husin, and S. K. Nguang, "Capacitive power transfer with impedance matching network," in *Proc. Int. Colloq. Signal Process. Appl.*, 2016, pp. 124–129.
[18] J. Dai and D. C. Ludois, "Capacitive power transfer through a conformal bumper for electric vehicle charging," *IEEE J. Emerg. Sel. Topics Power Electron.*, vol. 4, no. 3, pp. 1015–1025, Sep. 2016.
[19] B. H. Choi, D. T. Nguyen, S. J. Yoo, J. H. Kim, and C. T. Rim, "A novel source-side monitored capacitive power transfer system for contactless mobile charger using class E converter," in *Proc. IEEE Veh. Technol. Conf.*, 2014, pp. 1–5.
[20] L. Huang, A. P. Hu, A. Swain, and X. Dai, "Comparison of two high frequency converter for capacitive power transfer," in *Proc. IEEE Energy Convers. Cong. Expo.*, 2014, pp. 5437–5443.
[21] IEEE Standard for Safety Levels With Respect to Human Exposure to Radio Frequency Electromagnetic Fields, 3 kHz to 300 GHz, IEEE Std. C95.1, 2005.
[22] A. Kumar, S. Pervaiz, C. K. Chang, S. Korhummel, Z. Popvic, and K. Afridi, "Investigation of power transfer density enhancement in large air-gap capacitive wireless power transfer systems," in *Proc. IEEE Wireless Power Transfer Conf.*, 2015, pp. 1–4. doi: 10.1109/WPT.2015.7140182.
[23] I. Ramos, K. Afridi, J. A. Estrada, and Z. Popvic, "Near-field capacitive wireless power transfer array with external field cancellation," in *Proc. IEEE Wireless Power Transfer Conf.*, 2016, pp. 1–4. doi: 10.1109/WPT.2016.7498829.
[24] S. Li, Z. Liu, L. Zhu, C. Shuai, and Z. Chen, "Wireless power transfer by electric field resonance and its application in dynamic charging," *IEEE Trans. Ind. Electron.*, vol. 63, no. 10, pp. 6602–6612, Oct. 2016. doi: 10.1109/TIE.2016.2577625.
[25] F. Lu, H. Zhang, H. Hofmann, and C. Mi, "A high efficiency 3.3kW loosely-coupled wireless power transfer system without magnetic material," in *Proc. IEEE Energy Convers. Congr. Expo.*, 2015, pp. 2282–2286.

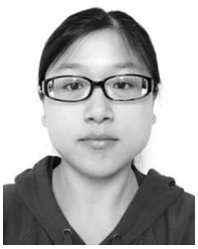

Hua Zhang (S'14) received the B.S. and M.S. degrees in electrical engineering, in 2011 and 2014, respectively, from the Northwestern Polytechnical University, Xi'an, China, where she is currently working toward the Ph.D. degree in electrical engineering.

From September 2014 to August 2015, she was a joint Ph.D. student founded by the China Scholarship Council with the University of Michigan, Dearborn. From September 2015, she started to work in San Diego State University, San Diego, CA, USA. Her research interest focuses on the coupler design of high power IPT and CPT system.

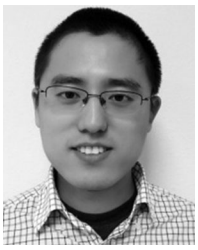

Fei Lu (S'12) received the B.S. and M.S. degrees in electrical engineering from the Harbin Institute of Technology, Harbin, China, in 2010 and 2012, respectively. He is currently working toward the Ph.D. degree in electrical engineering from the University of Michigan, Ann Arbor, MI, USA.

He is working on the high power and high efficiency capacitive power transfer through an air-gap distance up to 100s of millimeters. He is also working on the application of wide band-gap devices on wireless power transfer (WPT) system to increase the system frequency. His research interest focuses on WPT for the application of electric vehicle charging.

Heath Hofmann (M'98–SM'15) received the B.S. degree in electrical engineering from the University of Texas at Austin, Austin, TX, USA, in 1992, and the M.S. and Ph.D. degrees in electrical engineering and computer science from the University of California, Berkeley, CA, USA, in 1997 and 1998, respectively.

He is currently an Associate Professor with the University of Michigan, Ann Arbor, MI, USA. His research interests include the design, analysis, and control of electromechanical systems, and power electronics.

Weiguo Liu (SM'07) received the B.S. degree in electrical machines engineering from the Huazhong University of Science and Technology, Wuhan, China, and the M.S. degree in electrical engineering and the Ph.D. degree in control theory and control engineering from the Northwestern Polytechnical University, Xi'an, China, in 1982, 1988, and 1999, respectively.

He is a Professor in the Department of Electrical Engineering, Northwestern Polytechnical University, and a Guest Professor with the University of Federal Defense, Munich, Germany. He is the Director of the Institute of Rare Earth Permanent Magnet Electrical Machines & Control Technology, Northwestern Polytechnical University. His research interests include brushless dc machines, PM synchronous machines, dc machines, and induction machines.

Dr. Liu was the Chairman of Organizing Committee of the 32nd Chinese Control Conference, July 2013, Xi'an, China.

Chunting Chris Mi (S'00–A'01–M'01–SM'03–F'12) received the B.S.E.E. and M.S.E.E. degrees in electrical engineering from the Northwestern Polytechnical University, Xi'an, China, and the Ph.D. degree in electrical engineering from the University of Toronto, Toronto, ON, Canada, in 1985, 1988, and 2001, respectively.

He is a Professor and the Chair of electrical and computer engineering and the Director of the Department of Energy-funded Graduate Automotive Technology Education Center for Electric Drive Transportation, San Diego State University (SDSU), San Diego, CA, USA. Prior to joining SDSU, he was with with the University of Michigan, Dearborn, MI, USA, from 2001 to 2015. He was the President and the Chief Technical Officer of 1Power Solutions, Inc., from 2008 to 2011. He is the Co-Founder of Gannon Motors and Controls LLC and Mia Motors, Inc. He has conducted extensive research and has published more than 100 journal papers. He has taught tutorials and seminars on the subject of HEVs/PHEVs for the Society of Automotive Engineers (SAE), the IEEE, workshops sponsored by the National Science Foundation, and the National Society of Professional Engineers. He has delivered courses to major automotive OEMs and suppliers, including GM, Ford, Chrysler, Honda, Hyundai, Tyco Electronics, A&D Technology, Johnson Controls, Quantum Technology, Delphi, and the European Ph.D. School. He has offered tutorials in many countries, including USA, China, Korea, Singapore, Italy, France, and Mexico. He has published more than 100 articles and delivered 30 invited talks and keynote speeches. His research interests include electric drives, power electronics, electric machines, renewable-energy systems, and electrical and hybrid vehicles.

Dr. Mi received the "Distinguished Teaching Award," the "Distinguished Research Award" of University of Michigan, Dearborn, the 2007 IEEE Region 4 "Outstanding Engineer Award," the "IEEE Southeastern Michigan Section Outstanding Professional Award," and the "SAE Environmental Excellence in Transportation (E2T)." He has also served as a Panelist in major IEEE and SAE conferences.